Photoelectrochemical water splitting with ITO/WO_3/$BiVO_4$/CoPi multishell nanotubes enabled by a vacuum and plasma soft-template synthesis

Jorge Gil-Rostra [1]; Javier Castillo-Seoane [1]; Qian Guo [2]; Ana Belén Jorge Sobrido [2]; Agustín R. González-Elipe [1]; Ana Borrás [1]*

(1) Nanotecnology on Surfaces and Plasma Lab. Instituto de Ciencia de Materiales de Sevilla (CSIC-US). Avenida de Américo Vespucio, 49, 41092, Sevilla, SPAIN.

(2) School of Engineering and Materials Science, Queen Mary University of London, E1 4NS, London, UK

*Corresponding author: jorge.gil@icmse.csic.es

KEYWORDS: Photoelectrochemistry (PEC), water splitting, oxygen evolution reaction (OER), ITO, WO_3, $BiVO_4$, CoPi, multishell nanotubes (NTs), soft template synthesis, magnetron sputtering.

ABSTRACT

A common approach for the photoelectrochemical (PEC) splitting of water relies on the application of WO_3 porous electrodes sensitized with $BiVO_4$ acting as visible photoanode semiconductor. In this work, we propose a new architecture of photoelectrodes consisting of supported multishell nanotubes (NTs) fabricated by a soft-template approach. These NTs are formed by a concentric layered structure of indium tin oxide (ITO), WO_3, and $BiVO_4$, together with a final thin layer of cobalt phosphate (CoPi) co-catalyst. The photoelectrode manufacturing procedure is easily implementable at a large scale and successively combines the thermal evaporation of single crystalline organic nanowires (ONWs), the magnetron sputtering deposition of ITO and WO_3, and the solution dripping and electrochemical deposition of, respectively, $BiVO_4$ and CoPi, plus the annealing in air under mild conditions. The obtained NT electrodes depict a large electrochemically active surface and outperform the efficiency of equivalent planar-layered electrodes by more than one order of magnitude. A thorough electrochemical analysis of the electrodes illuminated with blue and solar lights demonstrates that the characteristics of the $WO_3/BiVO_4$ Schottky barrier heterojunction control the NT electrode efficiency, which depended on the $BiVO_4$ outer layer thickness and the incorporation of the CoPi electrocatalyst. These results support the high potential of the proposed soft-template methodology for the large-area fabrication of highly efficient multishell ITO/WO_3/$BiVO_4$/CoPi NT electrodes for the PEC splitting of water.

INTRODUCTION

The photoelectrochemical (PEC) splitting of water is considered one of the most important drivers towards the development of energy-sustainable methods for hydrogen production. [1-3] A widely investigated approach entails the application of efficient visible light semiconductor electrodes for the oxygen evolution reaction (OER). [4-7] From the materials' composition point of view, a classical option for this purpose consists of using electrodes formed by the WO_3 wide bandgap semiconductor sensitized with an external layer of $BiVO_4$, this latter acting as highly performant visible light scavenger semiconductor. [8-12] Besides enabling the sensitization with visible photons of the solar spectrum, this configuration contributes to overcoming some of the problems found by the implementation of WO_3 electrodes, namely a high photohole-photoelectron recombination rate and a considerable corrosion by intermediate peroxo-like species formed during the OER. [13] Therefore, much effort has been dedicated to the tailored synthesis of layered photo-electrodes through the stacking of these two semiconductors in configurations that maximize the effective interface area with the electrolyte. Among the rich literature on WO_3 and $WO_3/BiVO_4$ high area photoelectrode structures, we can quote nanoflakes and nanorods prepared by hydrothermal methods, [14 15] nanowires prepared by flame vapour deposition, [8 16-19], nanowires decorated by atomic layer deposition [20] or helix structures prepared by glancing angle evaporation, [21] this latter rendering the maximum efficiencies reported so far for this type of bilayer photoelectrodes (for a more complete appraisal of preparation methods and available structures, see the reviews in refs. [13 22]). However, despite the imperious need for large-area scalable methods compatible with common electrocatalyst supports, most reported manufacturing technologies have been tested at lab scale. [23] Addressing this challenge, herein we propose the use of a scalable methodology for the fabrication of substrate-supported nanotubes (NTs) with a multishell nanoarchitecture

consisting of an ITO inner layer covered with a $WO_3/BiVO_4$ heterojunction shell bilayer. This concentric architecture around the ITO layer provides a direct drainage pathway for the photoelectrons generated at the $WO_3/BiVO_4$ bilayer, thus minimizing the ohmic resistance to the external circuit. It will be also shown that the arrangement in the form of nanotubes, apart from the obvious enhancement in surface area in comparison with a planar thin film topology, provides a significant scattering of light that contributes to the light absorption capacity of the semiconducting shells.

In addition to the evaluation of the PEC activity of NT electrodes, a critical point for assessment in this work has been to determine the influence of the thickness and morphology of the outer $BiVO_4$ shell layer on the OER yield. Recently, Kafizas et al., [24] and Grigioni et al., [25] using transient absorption spectroscopy and planar $WO_3/BiVO_4$ thin film heterojunction electrodes, have shown that photocurrent dependens on $BiVO_4$ thickness, reaching a maximum yield for a thickness of 75 nm. Herein, we have compared the performance of the NT electrodes for a constant thickness of ITO and WO_3 layers, but variable $BiVO_4$ layer thickness. The impedance spectroscopy analysis of the OER photoelectrode's behaviour under blue light excitation [3 26-28] has provided some clues to understand the charge transfer mechanism at the $WO_3/BiVO_4$ interface and to determine the optimal $BiVO_4$ layer thickness. These results have been compared with those obtained with a thin film $ITO/WO_3/BiVO_4$ reference electrode, prepared by the same methodology but formed by the stacking of planar layers and that, therefore, depicted a much lower electrochemically active surface area. [11 29] The optimized NT topology has been also modified by the addition of a phosphate cobalt co-catalyst (CoPi) to further enhance the OER reaction efficiency. [30-34] Tested under one sun illumination, this electrode configuration rendered a PEC current of 2.23 mA/cm^2 for an applied voltage of 1.23 V vs. reversible hydrogen electrode (RHE). The obtained results

define a set of critical boundary conditions in terms of NT length, semiconductor layer thickness, and co-catalyst load that can be tailored to maximize the efficiency of this type of nanostructured electrodes.

PHOTOANODE FABRICATION METHODOLOGY

Scheme 1 (a) presents a conceptual representation of the synthesis steps required to produce the NT electrodes. The method is large-area compatible and, regarding the incorporation of the ITO and WO_3 layers, can be carried out in a single vacuum deposition reactor (i.e., following a one-reactor approach). [35] The fundamentals of the procedure rely on the use of small-molecule single-crystalline organic nanowires (ONWs) as soft-template 1D scaffolds, which can be fabricated and removed upon mild heating in vacuum or air. Although this work is the first example showing the application of this methodology for the fabrication of electrodes formed by a complex multilayered architecture (i.e., ITO/WO_3/$BiVO_4$), it has a general character and has been recently applied to other oxide materials and applications. [36] [37] In steps (*i-iii*), ONWs are formed by the self-assembly of pi-stacked small molecules such as porphyrins, perylenes, and phthalocyanines. The ONWs grow under defined vacuum and temperature conditions by evaporation of the molecules on the desired support with previously deposited ITO nuclei. In the present work, the ONWs were made by the stacking of commercially available H_2-phthalocyanine (H_2Pc) molecules. A detailed description of the mechanisms behind this fabrication process can be found elsewhere. [38] [39] A singular advantage of this procedure is its compatibility with a large variety of materials and substrates including polymers, soda lime glass, metallic meshs, ceramics, fabrics or paper, among others. In a subsequent step (*iv*) an ITO layer is deposited around the ONWs. For this step, we follow the procedure described in reference [35] where we have reported the fabrication by magnetron sputtering (MS) of ITO nanotubes (NTs) on a flat ITO substrate. MS is a well-

established industrially scalable technique usually employed for the fabrication of compact thin films and, more recently, also for porous structures of WO_3 electrodes [40] and $WO_3/BiVO_4$ photoelectrodes, [41 42] the former under an oblique angle configuration. The versatility of the MS procedure enables a conformal deposition of the ITO and then the WO_3 layers (step (*v)*) in the same reactor (see the Materials and Methods and Supporting Information sections for details). In step (*vi*), the multishell architecture is covered with a third layer of $BiVO_4$ deposited by drop casting. The annealing removal of the organic scaffold rendered substrate-supported multishell NT electrodes, which have been extensively characterized and photoelectrochemically tested. Scheme 1 (b) shows a cross-section representation of the sequential growth of the NT shell structure (steps (*iii*) to (*vi*)). It highlights that the NTs integrate a transparent conductive ITO core covered by concentric WO_3 and $BiVO_4$ layers. This configuration ensures a high surface area, the adjustment of the WO_3 and $BiVO_4$ semiconductor bands in line with the expected electronic behaviour of this heterojunction [9 13 16 22 30 42 43] and a minimization of the photoelectron path required to reach the ITO draining electron layer. As a final step in the preparation procedure, a very thin layer of cobalt phosphate (CoPi) is added by a photoelectrochemical-activated deposition technique (c.f. Scheme 1 (b) (*vii*)).

It is noteworthy that the synthesis procedure along the steps *(i)-(vii)* is quite versatile and permits a fine control of the electrode microstructure by, for example, varying the areal density of NTs (i.e., changing the ITO nucleation sites in step *(ii)*), the length of NTs (i.e., controlling the length of the ONWs through the adjustment of the evaporation time of the organic molecules in step *(iii)*) or the thickness of the different layers that constitute the multishell structure (i.e., modifying the MS deposition conditions in steps *(iv)* and *(v)*). This versatility would enable the optimization of electrode performance. In this work, besides analyzing the performance of a conventional PEC

electrode configuration, we have specifically addressed the dependence of PEC efficiency on the thickness of the $BiVO_4$ layer prepared in step *(vi)*.

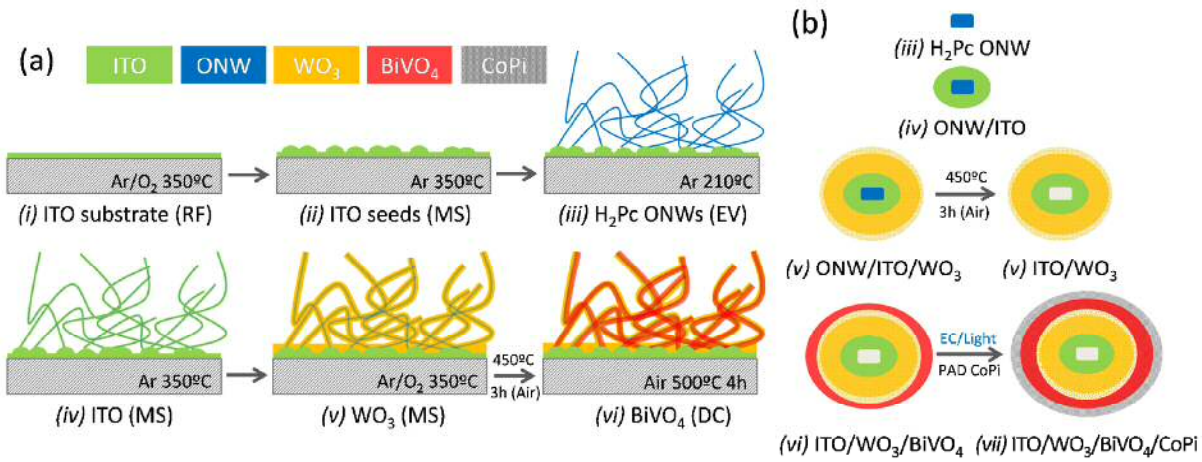

Scheme 1. *Conceptual schematic description (not to scale) of the multi-step synthesis procedure of the ITO/WO_3/$BiVO_4$ multishell NT photoanodes. (a) Synthesis steps of the NTs (steps i-vi) on an ITO glass substrate. (b) Scheme of the evolution of the NT cross section after the successive preparation steps (iii-vi) in (a), and after the incorporation of a Co phosphate co-catalyst (step vii) (see also Materials and Methods and Supporting Information S1 sections). RF indicates radio-frequency plasma pretreatment; MS magnetron sputtering; EV thermal evaporation; and DC drop casting.*

RESULTS and DISCUSSION

Characterization and optical properties of ITO/WO_3/$BiVO_4$ NT electrodes

In this section, we present a thorough description of the morphology, crystallinity, chemical composition and optical properties of the NT samples. Figure 1 shows a series of SEM micrographs illustrating the evolution of the ONWs and hollow NTs throughout the successive steps of the preparation protocol depicted in Scheme 1. These images are top-view micrographs at different

magnifications of the ONWs scaffold (Figure 1 (a)), firstly covered by the ITO shell (Figure 1 (b)) and then by the WO_3 shell (Figure 1 (c)). Figure 1 (c) also shows the effect of the annealing treatment to completely remove the organic core formed by the said ONWs. It will be demonstrated below that this thermal treatment also ensures the required stoichiometry and crystallization of the WO_3 shell. Figure 1 (c) presents the image of a sample with a shell structure ITO/WO_3, hereafter labelled as NT_#0 (cf. Materials and Methods section). Figures 1 (d) and (e) show selected SEM micrographs at two magnification scales taken after deposition and annealing of the $BiVO_4$ semiconductor layer (samples ITO/WO_3/$BiVO_4$, which are labelled as NT_#1, NT_#2, and NT_#3, depending on the equivalent thickness of the $BiVO_4$ layer). The lower magnification image of sample NT_#2 in Figure 1 (e) clearly shows that the electrodes are formed by supported NTs with an average surface density of 5-7 NTs/μm^2 and a maximum length of 10 μm. It should be noted that the length and thickness of NTs can be varied through the adjustment of the fabrication conditions of the ONWs (for the density and length, see refs [27] [28]) and the deposition time of the shell layers to effectively control their thickness. The choice of an average length in the order micrometres and a relatively low aereal density of ONWs was a compromise to maximize the conformality and thickness homogeneity of the shell layers prepared by MS along the length of the NTs. The comparison among Figures 1 (a)-(d) reveals that the twisted and flexible microstructure of the pristine organic ONW templates (Figure 1 (a)) transforms in a rather vertical arrangement of NTs when the ONWs become MS coated by ITO and then WO_3 (Figures 1 (b) and (c)). This evolution has been previously reported for TiO_2 and ZnO NTs fabricated by the same soft template approach using plasma-enhanced chemical vapour deposition. It has been attributed to the vertical alignment of the NWs under the effect of the electrical field lines of the plasma sheath and the increase of the rigidity of the NTs after coating with the metal oxide layer(s).[44]

Figures 1 (f) to (h) show a detailed electron microscopy analysis (i.e., including HAADF-STEM (f), bright-field TEM (g) images, and an HREM-diffraction pattern (h)) of a single nanotube retrieved from sample NT_#0 (Figure 1 (c)). This analysis shows the hollow space left in the interior of the NTs after the annealing removal of the ONW core (Scheme 1 (a) and (b), step (*v*)). Figure 1(f) shows that the empty core in the centre of the NTs is homogeneously surrounded by the ITO and WO_3 layers. It also reveals that the WO_3 outer shell was structured in the form of nanocolumns perpendicular to the core axis. This microstructure will likely provide a high surface area and therefore contribute to increasing the PEC activity of the electrodes. On the other hand, the bright field image in Figure 1 (g) demonstrates that the ITO/WO_3 interface is sharp and well-defined, while the high-resolution electron micrograph (HREM) in Figure 1 (h) proves the polycrystalline character of the grains and their random orientation. In this HREM image and the inset showing the electron diffraction diagram, it is also possible to recognize the diffraction features and interplanar distances typical of the crystalline planes of WO_3. It is also apparent in the image in Figure 1 (f) that the NT width slightly varies from the tip to the side through which it anchors onto the ITO substrate. This particular shape of NTs is a consequence of the MS growth mechanism during the deposition onto 1D scaffolds. [35] Depending on conditions, a part of the MS deposited particles may be ballistic and undergo shadowing effects during their trajectory from the target up to their landing position on the surface, preferentially accumulating at the outer parts of nanostructures. [45] To minimize this effect and therefore achieve a more homogeneous distribution of material along the NT length, deposition conditions should favour the particle randomization through collisions with the plasma gas molecules (essentially, this is achieved by increasing the plasma gas pressure and the distance target-substrate during deposition). [46]

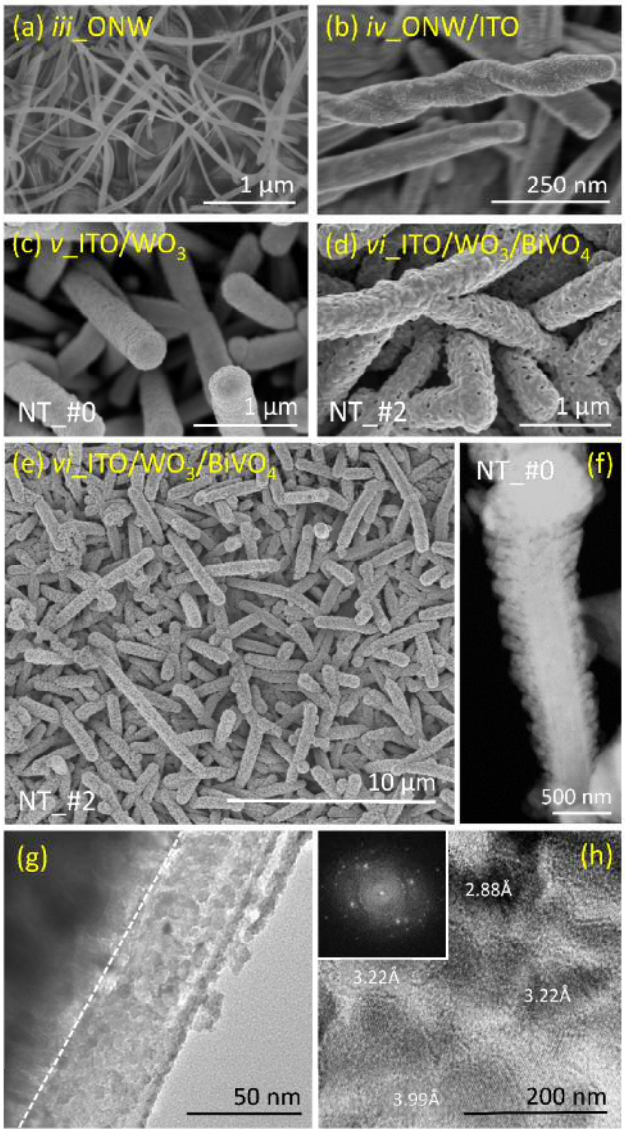

Figure 1. *(a)-(e) Selected top view SEM micrographs at various magnification scales of the hollow multishell NT samples at different stages of their manufacturing process according to Scheme 1. (f)-(h) Analysis of a single NT retrieved from sample NT_#0: (f) HAADF-STEM image, (g) bright field TEM image and (h) HREM-diffraction patterns. Please note that labels indicate the different steps (i-vi) detailed in Scheme 1.*

The next step of the photoanode manufacturing process consisted of the deposition of $BiVO_4$ by drop-casting (Scheme 1 (a), step (*vi*)). Figures 2 (a)-(e) show characteristic SEM micrographs, at low and high magnifications, of the NT structure of samples NT_#1, NT_#2 and NT_#3. Figure 2 (g) presents a HAADF-STEM image of an individual NT taken from sample NT_#1. This image proves that the microstructure of the $BiVO_4$ layer is formed by grains covering the NT outer surface (see Figure S1 in the Supporting Information section for better defined cross-section views of samples NT_#1 and NT_#3 obtained processing the single nanotubes by Focused Ion Beam (FIB). As expected, the average NT width increases with the amount of $BiVO_4$ (i.e., with the number of drop casting steps), reaching an average width higher than 500 nm in sample NT_#3. Micrographs in Figures 2 (a)-(f) demonstrate a progressive homogenization of the $BiVO_4$ layer from sample NT_#1 to sample NT_#3. Thus, in sample NT_#1, $BiVO_4$ forms a very thin layer (thickness in the order of a few tenths of nanometers), which fills the porous structure of the WO_3 layer beneath, together with small imperfectly coalesced aggregates. EDX maps in Figure S1 confirm that $BiVO_4$ spreads relatively well onto WO_3 in sample NT_#1, while in samples NT_#2 and NT_#3, this compound forms large aggregates, which are partially connected in a kind of granular shell (Figures 2 (c) to (f)).

Although an accurate estimation of the NT thickness is hampered by the inherent random distribution of sizes of these structures, a statistical analysis of the SEM images taken at medium magnifications at selected representative areas of samples (see data gathered in Table S1 of the Supporting Information) gives the following average values of NT width: 438 ± 64 nm (sample NT_#0), 483 ± 35 nm (sample NT_#1), 568 ± 78 nm (sample NT_#2) and 582 ± 48 nm (sample NT_#3). These measurements render approximate $BiVO_4$ layer thickness of 30 nm, 65 nm and 85 nm for samples NT_#1, NT_#2 and NT_#3, respectively. For comparison, the mean thickness

values of the WO_3 and $BiVO_4$ layers stacked in sample TF, estimated from the cross-section micrograph in Figure S2, were 550 nm and 370 nm, respectively**.**

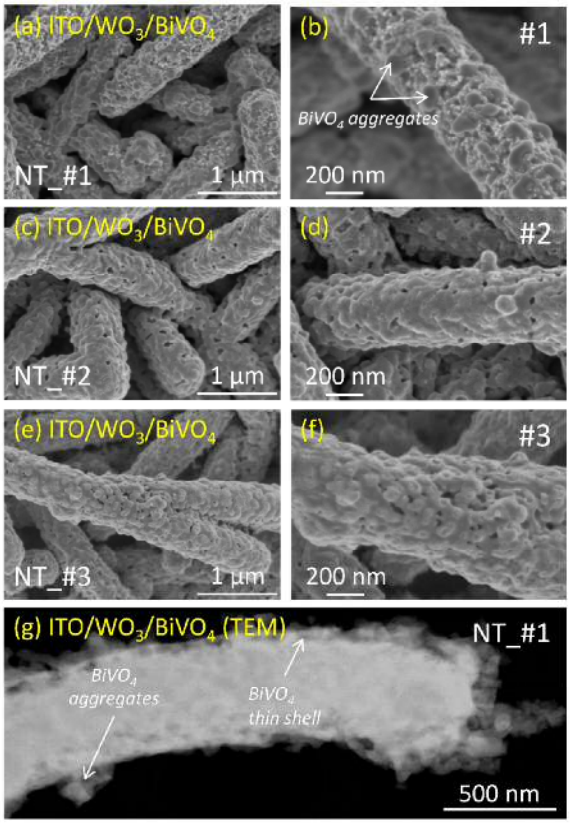

Figure 2. *(a)-(f) Top view SEM micrographs at two different magnifications (1µm and 200 nm scale) of the multishell NTs, for increasing amounts of $BiVO_4$ from samples NT_#1, NT_#2 to NT_#3, as labelled. (g) HAADF-STEM image of a single NT taken from sample NT_#1.*

The crystal structure of WO_3 and $BiVO_4$ semiconductors is of paramount importance for a proper operation of $WO_3/BiVO_4$ heterojunction photocells. [8-12 16 22 42 43] An analysis of the crystallinity of the NT electrodes by XRD rendered the diagrams in Figure 3 (a) for samples NT_#0, NT_#1, NT_#2 and NT_#3. These diagrams depict the typical peaks of well-crystallized ITO (cubic structure), WO_3 (monoclinic structure), and $BiVO_3$ (monoclinic structure). [47-49]

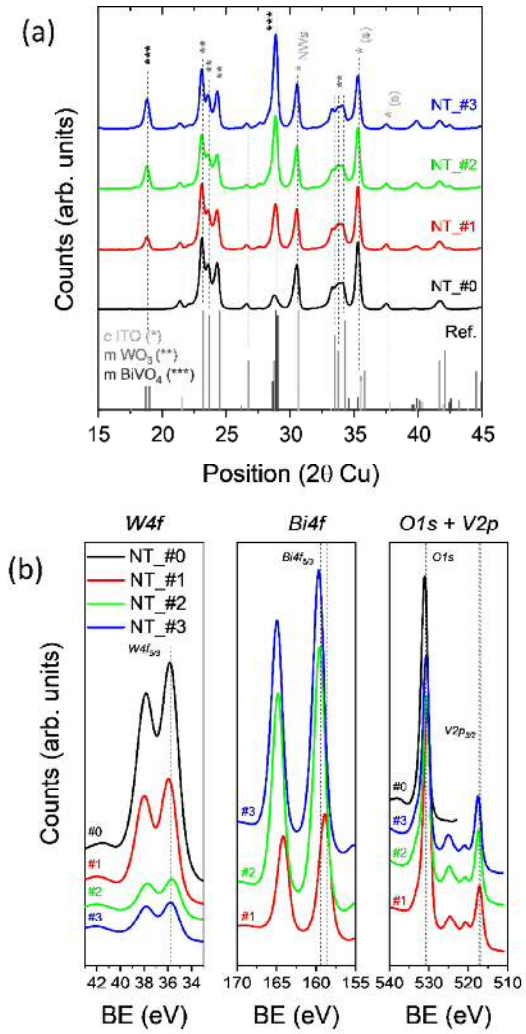

Figure 3. a) *XRD diagrams for samples NT_#0 to NT_#3. Peaks attributed to the cubic structure of In_2O_3/SnO_2 (*)* [47] *the monoclinic structure of WO_3 (**)* [48] *and the monoclinic structure of $BiVO_4$ (***)* [49] *can be identified in the diagrams. b) W4f, Bi4f and O1s/V2p high resolution XPS spectra of samples NT_#0, NT_#1, NT_#2 and NT_#3.*

The deposition of $BiVO_4$ by drop-casting and the chemical nature of the surface of NTs were investigated by XPS and EDX. The comparison of low resolution XPS spectra reported in Figure S3 shows a progressive decrease of the W4f/Bi4f intensity ratio when passing from sample NT_#0

to samples NT_#1, and NT_#2, while differences in this parameter were smaller when comparing samples NT_#2 and NT_#3. This evolution confirms the aforementioned SEM observations in the sense that the coverage of $BiVO_4$ onto the WO_3 shell is rather conformal in samples NT_#1 and NT_#2, while in sample NT_#3, there is a certain agglomeration of this compound in the form of relatively big clusters. The fact that the W4f signal is still visible in samples NT_#1, NT_#2 and even NT_#3 also indicates that some zones of WO_3 are not completely covered by $BiVO_4$. Meanwhile, the series of high resolution XPS spectra gathered in Figure 3 (b), besides supporting this assessment about coverage based on the low resolution spectra, confirm that W^{6+}, Bi^{3+} and V^{5+} are the oxidation states of these elements in the examined samples (B.E.s W4f (36 eV), Bi4f (159 eV) and V2p (517 eV)). In this regard, a deeper analysis of the O1s high resolution XPS spectra (see Supporting Information, Figure S3) leads to the attribution of its components to lattice oxygens in WO_3 (O-W) for sample NT_#0 and to an oxygen coordination environment in $BiVO_4$ (O-V) for samples NT_#1-#3, respectively, which confirms the previous NTs surface composition assessment.

In parallel to the changes outlined above on morphology and surface chemistry, samples underwent colour changes after each processing step. In particular, a white-yellow transformation was observed between steps (*v*) and (*vi*). This colour change must respond to the different diffuse reflectance spectra of samples NT_#0 (with only ITO and WO_3 layers) and NT_#1 to NT_#3, in these latter after the incorporation of $BiVO_4$ (see Supporting Information, Figure S4). Most remarkable in these spectra is the shift in the absorption edge from sample NT_#0 (approximately 2.7 eV) to samples NT_#1-#3 (approximately 2.4 eV for the three samples). This shift proves that the incorporation of $BiVO_4$ produces the yellow colouration of samples due to the capacity of this semiconductor to absorb visible light in the wavelength interval comprised between,

approximately, 400 and 450 nm. Most PEC experiments described next were done illuminating the photoanodes with photons with a wavelength within this energy window, i.e., to selectively inducing the excitation of the $BiVO_4$ semiconductor.

It will be shown in the next section that electrode samples NT_#1-#3 depict PEC efficiencies that are orders of magnitude higher than that of the reference thin film sample (TF). Such an improvement in photocurrent will likely depend on the increase in the surface area provided by the NT structure of samples NT_#1-#3, although a certain enhancement in light scattering due to the random arrangement of NTs may also contribute to increasing the photocurrents [3] (we have recently reported on a significant light scattering for NT structures of ITO). [35] The critical role of the high surface area of samples NT_#0-#3 working as photoanodes and its effect on the photocell efficiency was confirmed by determining their effective electrochemically active surface area (ECSA). [50-54] For this purpose, we applied the double-layer capacitance method to deduce capacitance values from the slope of current density vs. scan rate plots (see Supporting Information Figure S5). As expected, the obtained values for the multishell NT electrodes (see Figure S5) were almost two orders of magnitude higher than for the reference TF, thus confirming the importance of ECSA for an effective control of photo-efficiency. Interestingly, it was also found that the incorporation of $BiVO_4$ did not significantly modify the capacitance values of NT samples, thus indicating that samples NT_#0 to NT_#3 exhibited rather similar ECSA values.

PEC activity of thin film, multishell NTs and CoPi-modified electrodes.

Voltammetric and chronoamperometric tests were carried out with the NT and NT-CoPi photoelectrodes to assess their PEC activity in comparison with that of the TF samples. Most tests were carried out upon illumination with a 6500K LED, although experiments were also performed

under illumination with a solar simulator to determine the response of the most efficient NT electrodes according to standardized procedures. [55]

The PEC performance of NTs and TF electrodes was first assessed by linear sweep voltammetry (LSV) analysis. Figure 4 (a) shows the LSV curves measured for samples NT_#0-#3 and TF under illumination with the blue light of a 6500K LED (see Materials and Methods section) for a light flux power of 100 mW cm^{-2}. Samples NT_#0 and TF present a much lower PEC efficiency than samples NT_#1 to NT_#3. This difference must be attributed to the lack of the sensitizing $BiVO_4$ semiconductor layer in sample NT_#0 and the significantly lower ECSA and light scattering capacity in the reference TF sample. Meanwhile, a comparison among samples NT_#1 –_#3 shows that efficiency is maximum for sample NT_#2. A more complete LSV analysis of the PEC response of multishell NT electrodes as a function of the light flux (provided by a high intensity LED 6500K light source) is reported as Supporting Information, Figure S6. This complementary analysis revealed that current density did not saturate, even for light intensities as high as 300 mW/cm^2, and that for this high photon flux, the PEC currents determined for samples TF and NT_#0 were comparatively very small.

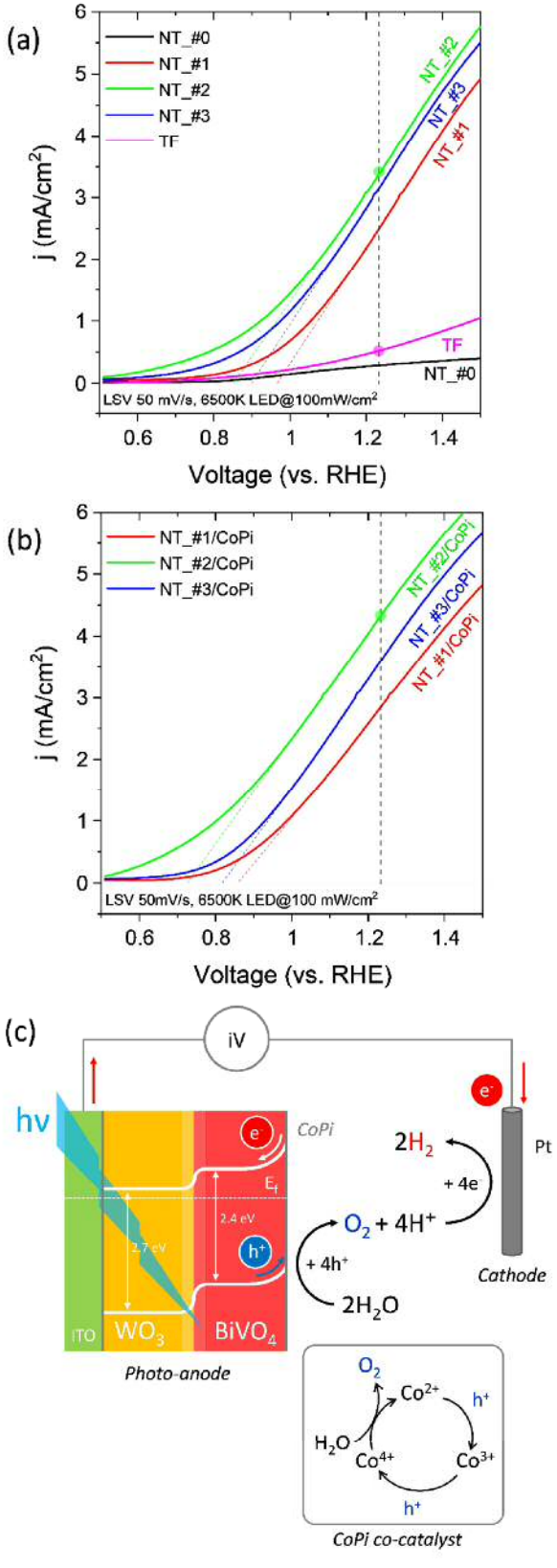
(a)
NT_#0
NT_#1
NT_#2
NT_#3
TF
j (mA/cm²)
LSV 50 mV/s, 6500K LED@100mW/cm²
Voltage (vs. RHE)
(b)
NT_#1/CoPi
NT_#2/CoPi
NT_#3/CoPi
LSV 50mV/s, 6500K LED@100 mW/cm²
Voltage (vs. RHE)
(c)
iV
hv
e⁻
CoPi
E_f
2.4 eV
2.7 eV
h⁺
ITO
WO3
BiVO4
Photo-anode
2H2
+ 4e
Pt
O2 + 4H+
+ 4h⁺
2H2O
Cathode
O2
Co2+
h⁺
H2O
Co4+
Co3+
h⁺
CoPi co-catalyst

Figure 4. *LSV analysis of NT electrodes under LED 6500K blue light (420-475 nm) illumination. (a) LSV diagrams under illumination withLED 6500K blue light for multishell NTs (i.e.NT_#0, NT_#1-#3) and TF-electrodes. (b) LSV diagrams under illumination with LED 6500K blue light for NT_#1/CoPi, NT_#2/CoPi and NT_#3/CoPi electrodes. (c) Band diagram describing the fate of photoelectrons and photoholes upon light absorption by the $BiVO_4$ semiconductor. Inset: schematic description of the catalytic mechanism of the CoPi co-catalyst to activate the OER.*

The observed photocurrents of samples NT_#1-#3 are linked to the visible absorption capacity of the $BiVO_4$ layer. According to common models of photoexcitation of sensitizing semiconductors, [8-12] photon absorption by $BiVO_4$ produces electron-hole pairs. As shown in the scheme in Figure 4 (c), the Schottky band bending of the $BiVO_4$ semiconductor at the water-photoelectrode interface promotes the migration of the photoholes to the surface where they react with water to yield a series of very reactive intermediate species (e.g., OH*, OOH*, O*), [56 57] which upon subsequent reactions lead to the generation of O_2. Meanwhile, the photo-electrons promoted to the conduction band diffuse to the conduction band of WO_3 and, then, through the ITO conductive layer, to the external circuit and eventually to the cathode where they chemically reduce water to hydrogen. The high efficiency found for this process with the NT electrodes supports a good matching at the heterojunction between the conduction bands of the two semiconductors (see Figure 4 (c)). In addition, the particular architecture of the NT photoanodes makes that photoelectrons only need to diffuse through the WO_3 shell thickness to find the ITO draining layer, i.e., through a short path, therefore reducing the ohmic resistance associated to the transport of electrons. Interestingly, equivalent experiments with green and red LEDs (emissions centred at 520 nm and 635 nm, respectively) did not produce any significant PEC reaction, in agreement with the negligible photon absorption coefficient of $BiVO_4$ at these wavelengths (data not shown).

The OER efficiency further increased when the NTs were decorated with the CoPi catalyst applied using a rather standard procedure. The LSV plots recorded in Figure 4 (b) for samples NT_#1/CoPi to NT_#3/CoPi reveal an increase in current density for these three samples compared to the equivalent ones without the OER co-catalyst (i.e., NT_#1-#3). It is known that the OER catalytic activity of cobalt catalysts involves the formation at high positive voltages (V>1.23 V vs. RHE) of Co^{3+} and Co^{4+} intermediate species, the latter in the form of CoO(OH) units (see the scheme in the insert of Figure 4). [58] Interestingly, the plots in Figure 4 (b) reproduce the order in efficiency found for the NT electrodes without catalyst, i.e., #2/CoPi > #3/CoPi>#1/CoPi.

The order in efficiency deduced from the LSV analysis (i.e. samples #2> #3 > #1) was confirmed by long-term chronoamperometry tests (CA). Figure 5 (a) shows the CA curves recorded as a function of time for an applied voltage of 1.23 V vs. RHE. Please note that these results correspond to the NT electrodes with the CoPi co-catalyst, although the same trend was also obtained without the co-catalyst. According to these curves, the photocurrent intensity depicts an initial increment for the first 30 min, followed by a smooth decrease during 3 hours. A similar behavior [59] has been attributed to the effective initial formation of Co^{3+} and Co^{4+} species during the first activation period, followed by a subsequent stabilization process. [59]

The summary of average photocurrent values gathered in Supporting Information Figure S7, determined by the LSV and CA experiments in Figures 4 and 5 for the NT electrodes with and without CoPi, confirms that samples NT_#2 and NT_#2/CoPi depict maximum efficiencies. Interestingly, when the used samples were taken out of the liquid medium, dried, and stored for three months to then perform a new experiment, the current density vs. time trend depicted in Figure 5 (a) was completely reproducible. This result confirms the stability and robustness of the NT electrodes and their long-lasting stability. The photon-assisted character of the electrolysis and

the long-term stability of this process was confirmed by complementary CA tests where the light provided by the 6500K LED was systematically chopped at small time intervals. Figure 5 (b) illustrates the results of an experiment carried out with sample NT_#2/CoPi. This figure shows that current is illumination-dependent and that current intensity after multiple chopping processes always recovers the value upon illumination without any significant decrease.

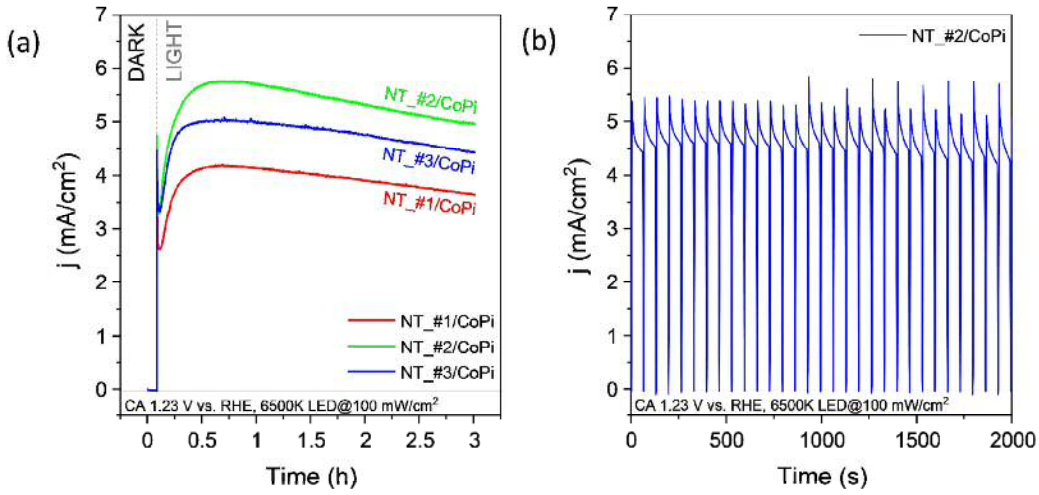

Figure 5. *Chronoamperometry tests of NT electrodes with CoPi co-catalysts. (a) CA diagrams at 1.23 V vs. RHE and a LED 6500K light source power flux of 100 mW/cm² recorded during a period of 3 h for samples NT_#1/CoPi, NT_#2/CoPi and NT_#3CoPi. (b) CA curves obtained under the same experimental conditions for sample NT_#2/CoPi while chopping the illumination approx. every 60 s.*

The analysis of the CA plots in Figure 5 (b) can be used to estimate transient times for the photo-hole migration through the $BiVO_4$ semiconductor. According to the works in refs., [58 60] the analysis of the initial transient decay up to stabilization of the current curve (see Supporting Information, Figure S8) can provide an estimate of the average diffusion time of photo-holes in their path

towards the surface. The diffusion time (τ) can be obtained through the following expressions: [60] [61]

$$lnD = -\frac{1}{\tau}t \quad \text{(Eq. 1)}$$

$$D = \frac{j(t)-j_f}{j_f-j_i} \quad \text{(Eq. 2)}$$

Where D can be determined experimentally as indicated in Figure S8. Calculated values of the diffusion time (τ) amounted to 9.5 μs for sample NT_#0 (note, however, the small current generated with this electrode, c.f, Figure 5 (a) and Figure 6 (a)) and 12.8 μs for the three multishell NT_#1/CoPi-#3/CoPi electrodes. These values are in good agreement with those previously reported for other nanostructured electrodes of these materials. [22] [60] [61] The similar photo-hole diffusion values found for the three multishell NT electrodes suggest that the observed differences in efficiency must involve additional factors, such as differences in reaction kinetics at the electrode interface or in other charge transfer phenomena that will be discussed in the next section.

LSV diagrams for electrodes NT_#2, NT_#2/CoPi and NT_#0 were also recorded under 1 sun illumination with a standard AM1.5 G solar simulator lamp (see details in the methods section). This experiment aimed at properly comparing according to standard methods [55] the photocurrents rendered by NT electrodes with those reported in the literature for other electrode configurations.[8-12] According to Figure 6 (a), upon illumination with the complete solar light spectrum, the electrode NT_#0 provides a low current density, although the intensity was significantly smaller than that measured with electrode NT_#2. Figure 6 (a) also shows a net increase in efficiency when incorporating the CoPi co-catalyst (i.e., for sample NT_#2/CoPi), photocurrent amounting to a maximum of 2.23 mA/cm^2 at 1.23 V vs. RHE. Although this value is still far from the maximum

values reported for other nanostructures of the same materials [13] [21] [41] it is in the order of recent efficiencies reported for nanostructures resembling those used in the present work, though prepared by other methods. [22] We expect that the versatility of the template methodology applied in the present work and the basic information about semiconductor heterostructures deduced here will permit further improvements in efficiency. It is also noteworthy that the threshold potential for the OER, determined by a simple extrapolation of the j vs.V curve, presented a remarkably low value of 0.63 V for this electrode. On the other hand, the incident photon to current conversion efficiency (IPCE) curves and the integrated solar photocurrent curves (AM1.5 G) gathered in Figure 6 (b), taken at a voltage of 1.0 V vs. RHE reference electrode, confirm that samples NT_#2 and NT_#2/CoPi are effectively sensitized with λ<500 nm photons, while sample NT_#0 only presents photoresponse for λ<450 nm photons.

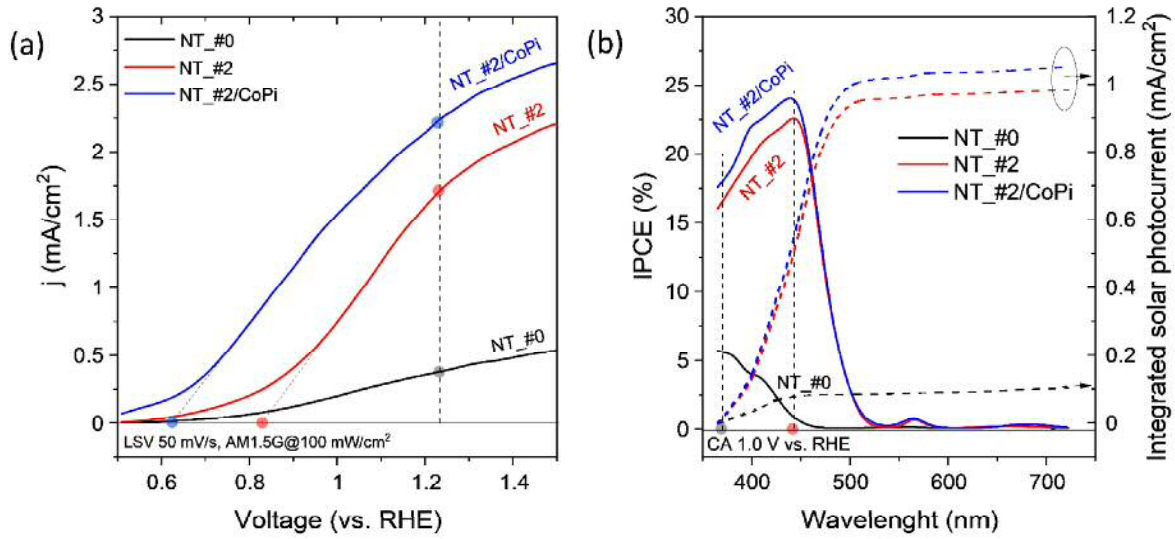

Figure 6. *(a) Electrode sensitization under illumination with a standard 1 sun solar simulator (AM1.5 G). LSV plots correspondint to samples NT_#0, NT_#2, and NT_#2/CoPi. (b) IPCE curves,*

and integrated solar photocurrent (AM1.5 G) (dashed lines) taken at 1.0 V (vs. RHE) for these same electrode samples.

Electrode morphology and charge transfer processes at the NT electrode-electrolyte interface

To further account for the impact of NT morphology on PEC cell efficiency, we have characterized the cell electrical behaviour by electrochemical impedance spectroscopy (EIS) and analyzed the charge transfer kinetics at the interface using Tafel analysis, either with or without CoPi co-catalyst. As a result, we have gained a better understanding of the main factors contributing to the high efficiency of the NT electrodes and, in this way, unravel the mechanisms promoting samples NT_#2 and NT_#2/CoPi as the most efficient photoelectrodes.

Nyquist plots obtained by EIS are reported in Figure 7 (a). These plots can be fitted by assigning specific values to the electrical elements of the equivalent circuit included as an insert in this figure. Similar types of circuits have been proposed to account for the charge transfer behaviour in other $WO_3/BiVO_4$ nanostructured heterojunction electrodes. [26-28]

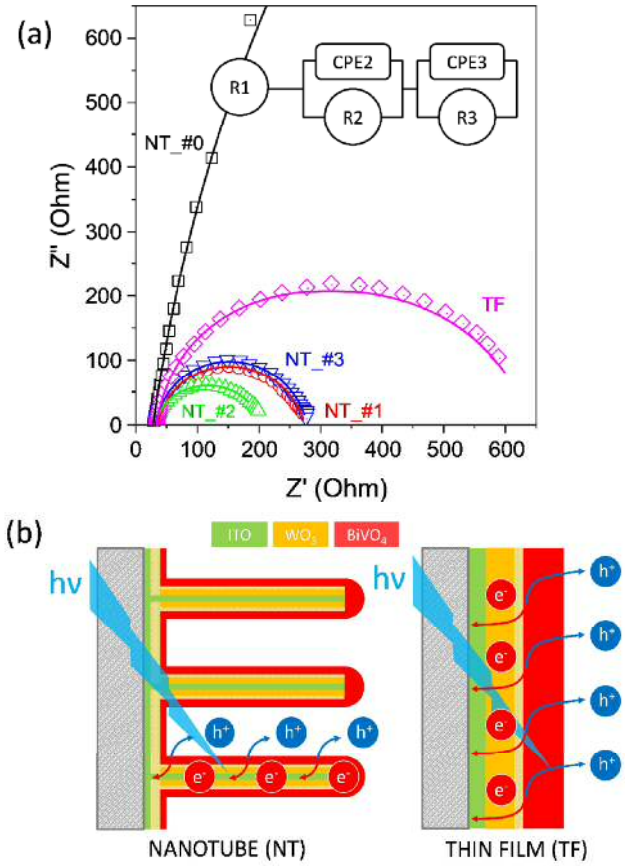

Figure 7. *(a) Nyquist plots for samples NT_#0-#3 and TF-recorded under 6500K LED illumination with an intensity of 100 mW/cm^2 and an applied voltage of 1.23 V vs. RHE. Inset: scheme of the equivalent circuit. (b) Scheme of the NT and TF electrode nanostructures and the involved PEC process, highlighting the operative advantages of the ITO/WO_3/$BiVO_4$ nanotube structure.*

The equivalent circuit incorporates three elements: i) element 1 characterized by a resistance R1, which is attributed to the resistance of the electrolyte solution, wires, clips and ITO substrate layers; ii) element 2, consisting of a resistance R2 and a constant phase element CPE2 that respond to the effect of the interfaces created between the semiconductor oxides integrated into the NTs and TF samples; iii) element 3, including a resistance R3 and a constant phase element CPE3 that

account for the charge transfer at the $BiVO_4$/electrolyte interface upon light illumination. Phase constant elements instead of pure capacitance elements are used in the scheme because of the non-linearity effects appearing at heterogeneous and nanostructured surfaces and interfaces. [26 62 63] The impedance associated with the CPEs can be formulated according to:

$$CPE = \frac{1}{Q\,(i\omega)^n} \qquad \text{(Eq. 3)}$$

where Q is a CPE parameter expressed in F·s, n is a number between 1 and 0, and ω is the angular frequency. The set of Nyquist plots reported in Figure 7 has been fitted using the parameters summarized in Table 1 (for the quality of fitting results see the continuous lines in Figure 7 (a)). These parameters encompass calculated values of resistance R, Q (directly related to the characteristic non-ideal capacitance of the said element), and an ideality factor (n) for each constant phase element.

Table 1. *Fitting parameters reproducing the shape of the Nyquist plots recorded at 1.23 V vs. RHE under LED 6500K illumination (100 mW/cm^2).*

		NT_#0	**NT_#1**	**NT_#2**	**NT_#3**	**TF**
	R1 (*Ohm*)	28.2	35.3	31.75	32.3	33.6
	R2 (*Ohm*)	2011.4	204.9	150.4	147.7	429.5
	R3 (*Ohm*)	2530.5	34.7	22.5	98.3	175.4
CPE2	Q2 ($F{\cdot}s/10^{-4}$)	2.4	3.0	4.7	5.1	5.0
	n2	1.00	0.82	0.79	0.85	0.81
CPE3	Q3 ($F{\cdot}s/10^{-4}$)	2.3	3.8	3.9	3.2	2.0
	n3	0.86	1.01	1.01	0.93	0.99

R1 parameter is rather similar for the studied samples, confirming its attribution to the overall electrical resistance of electrolyte plus other ohmic elements in the external circuit between the photoanode and cathode. [26] On the other hand, R2 and R3 and their sum are more than one order of magnitude higher for electrode NT_#0 than for the other NTs and TF electrodes, proving that the incorporation of a $BiVO_4$ outer layer is responsible for the photogeneration of charge upon blue light excitation. CPE2 and CPE3 are also higher for these electrodes than for electrode NT_#0. It is also remarkable that R2+R3 values for NT electrodes are much smaller than for TF electrodes, supporting the dependence of the PEC activity on the effective ECSA available in each case. In line with the proposal in previous sections, an additional factor contributing to reducing the value of R2+R3 for the NT electrodes must be the straightforward collection of photogenerated electrodes by the inner ITO layer extending along the whole nanotube structure. In summary, as schematized in Figure 7 (b), we claim that the core-shell ITO/WO_3/$BiVO_4$ nanostructure of the NT electrodes offers simultaneously a high electrochemical surface for the OER and minimum electrical resistance losses due to its particular core-shell configuration. The scattering of light within the NT structure is another factor contributing to increase the photocurrent. [35]

A Tafel analysis, based on the Butler-Volmer equation, [54] has been also applied to estimate the kinetics of charge transfer processes at the electrode-electrolyte interface. Figure 8 (a) shows a series of Tafel plots determined for the NT, NT-CoPi and TF electrodes. Assuming that the majority of photoholes arriving at the surface ends up in the photooxidation of water, the slope of these plots can be taken as a measure of the kinetics of the charge transfer processes at the interface. According to this figure, slopes of electrodes NT_#0 to NT_#3 are quite similar but bigger than that determined for electrodes NT_#1/CoPi to NT_#3/CoPi, clearly indicating that the addition of the CoPi co-catalyst favours the surface reaction between photoholes and water. The Tafel slope

for sample TF was higher than for NT electrodes, supporting that photoholes in this structure present a lower reactivity to generate O_2 molecules. This result is consistent with the lower photocurrent efficiency found for the TF configuration (see Figure 4), which is also clearly related to the significantly low ECSA values depicted by sample TF s (see Supporting Information, Figure S5). It is noteworthy at this point that, despite the similar Tafel slopes for electrodes NT and NT-CoPi, log j at a given potential follows the order #2>#3>#1 (and similarly for their equivalent electrodes with CoPi). Since the photohole diffusion times determined according to equation (1) (see the previous section and Supporting Information, Figure S8) were similar for the three NT electrodes and so was the reaction kinetics of photoholes inferred by the previous Tafel slope analysis (c.f., Figure 8), the maximum efficiency found for sample NT_#2 (and NT_#2/CoPi when incorporating the co-catalyst) suggests that the number of photo-holes arriving at the surface reaction sites is higher for this particular electrode.

We propose that the observed variation of efficiency with the $BiVO_4$ load is due to the relation between the length of the depletion layer (i.e, the length of the Schottky barrier defined by the band bending zone) and the equivalent thickness of the $BiVO_4$ sensitization layer/aggregates in samples NT_#1-NT_#3. According to the schemes in Figure 8 (b), the semiconductor sensitizing layer/aggregate in sample NT_#2 would have a thickness equivalent to the Schottky barrier length, thus enabling its complete development through the semiconducting layer. Under such conditions, all photogenerated charges would experience the electrical field of the band curvature enabling a more efficient separation of photogenerated electrons and holes and, consequently, diminishing photoelectron-photohole recombination probability. A similar effect was reported by us to account for the enhancement of photocatalytic activity in a rutile-anatase bilayer system. [64] Interestingly, the average thickness determined for this layer by the statistical morphological analysis of NTs in

sample NT_#2 is about 65-85 nm, within a similar range of values to that found by Selim et al., [24] or Grigioni et al. [25] as optimal thickness for a stable and efficient photoresponse in $WO_3/BiVO_4$ flat layer photoelectrodes. According to the scheme in Figure 8 (b), the equivalent thickness of the $BiVO_4$ semiconductor layer/aggregates in sample NT_#1 (ca. 35 nm, see Figure 2 and Table S1) would be smaller than the charged space length, making light absorption and photoelectron/photohole separation less effective. Meanwhile, in sample NT_#3, the bigger size of $BiVO_4$ aggregates (see discussion in Section 2.1) would be higher than the Schottky barrier length, making more probable the recombination of photogenerated electrons and holes in the flat zone of bands.

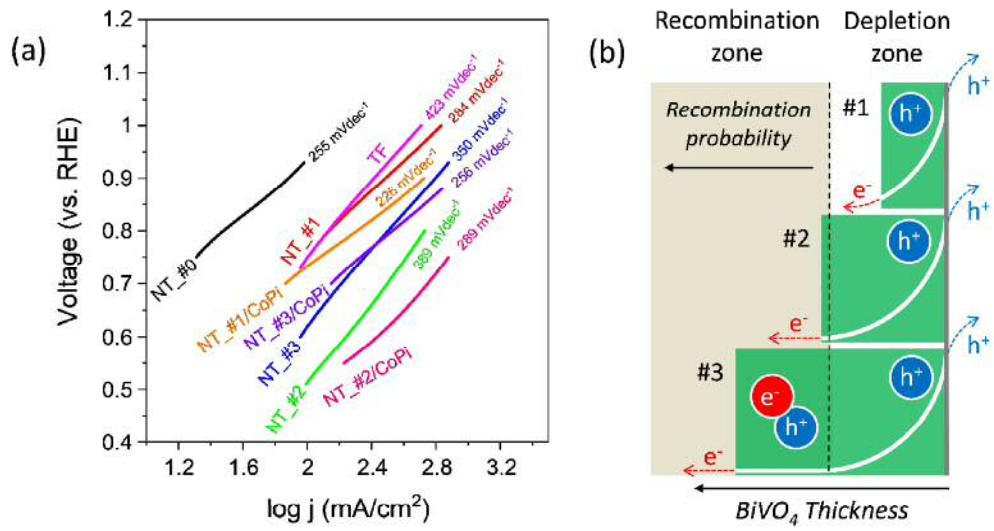

Figure 8. *Analysis of the charge transfer process at the electrode/electrolyte interface. (a) Tafel plots for NT, NT/CoPi and TF electrodes. (b) Band bending schemes for samples NT_#1, NT_#2 and NT_#3 taking into account an estimated thickness of $BiVO_4$ layer/aggregates and how charges diffusion and recombination would be affected by the electrical field of the Schottky barrier in each case.*

MATERIALS AND METHODS

Synthesis of multishell NT photoelectrodes

The multishell NT electrodes were manufactured following the steps described in Scheme 1. Deposition conditions of ITO and WO_3 layers by MS and the processing conditions of $BiVO_4$ coatings and CoPi layers by, respectively, solution dripping or electrochemical methods, are detailed in Supporting Information section S1. We used a commercial glass plate covered by ITO layers as substrates (supplied by Ossila, 400 nm thickness, 15 Ω/□). ITO substrates were ultrasonically bath-cleaned following a standard sequence of acetone, ethanol and deionized (DI) water solvents. Once in the vacuum chamber, the substrates underwent a cleaning and surface activation process by a mild radio frequency (RF) plasma treatment in an O_2/Ar atmosphere (step (*i*) in Scheme 1 (a)). Small ITO nuclei were additionally deposited by MS for very short times (step (*ii*)) to serve as nucleation sites for the formation of crystalline phthalocyanine ONWs (step (*iii*)). Details of the experimental procedure for the formation of the ONW templates by thermal evaporation can be found in previous publications [35 38 39] (see also Supporting Information section S1). Then, ITO was deposited by MS under conditions leading to the formation of a conformal layer completely covering the ONW templates (step (*iv*)). The MS deposition of ITO was followed in the same chamber by the MS deposition of WO_3 (step (*v*)). The steps described so far have been adopted following a one-reactor approach, i.e. using thermal evaporation and magnetron sputtering deposition following a one-reactor vacuum chamber premises. This protocol enables a rapid deposition avoiding the exposure to ambient conditions of the successively formed surfaces, as required in large-scale processes to prepare finely controlled interfaces. After vacuum deposition, ITO/WO_3 structures were annealed in air at 450 ºC for 3 h to achieve the complete removal of the

organic scaffold at the core of the NTs and to induce the crystallization of the WO_3 semiconductor oxide (step (*v*)).

$BiVO_4$ was incorporated onto a mask delimited substrate area of 1.1 cm^2 by sequentially dripping increasing volumes (i.e. 20, 40, 60 µl) of a solution of $BiNO_3x5H_2O$ (50 mM), $VO(acac)_2$ (46.5 mM) in an acetic acid/ethyl acetate (9.5/0.5) mixture as solvent. The dripping process was repeated up to three times to check the influence of the amount of $BiVO_4$ on the photo-efficiency of the electrodes. After the complete removal of the solvent (at room temperature) the samples were annealed in air at 500 ºC for 4 h to induce the complete crystallization of $BiVO_4$ and promote the $WO_3/BiVO_4$ heterojunction formation (see step (*vi*)). The final result was the hollow multishell NT structure described in Scheme 1 (b) step (*vi*), where the $BiVO_4$ shell semiconductor appears externally covering the WO_3 and ITO concentric shells. The set of fabricated $WO_3/BiVO_4$ photoelectrode samples are named as NT_#0 for the ITO/WO_3 NTs, and NT_#1, NT_#2, and NT_#3 for the ITO/WO_3/$BiVO_4$ NTs. A reference flat thin film sample (TF) was prepared in the form of stacked thin films by direct MS deposition of the multilayers onto a flat ITO substrate with no ONW scaffold followed by dripping 40 ml of the $BiVO_4$ precursor solution.

The cobalt phosphate (CoPi) co-catalyst was deposited using a light-stimulated electrochemical deposition method. [34] The NT_#1-NT_#3 electrodes were back-illuminated for 600 s with the light provided by a LED 6500K lamp (100 mW/cm^2) in a solution of 0.15 mM $Co(NO_3)_2x6H_2O$ in a 0.1 M potassium phosphate buffer (at pH=7.0) at a constant voltage of 0.4 V (vs. Ag/AgCl (3M KCl) reference electrode). Following the proposed notation, the CoPi set of samples has been labelled as NT_#X/CoPi (X: 1, 2 and 3).

Characterization of multishell NT photoelectrodes

The microstructure of the NTs was characterized by scanning electron microscopy (SEM) and transmission electron microscopy (TEM) together with EDX analysis, the latter to ascertain the layered structure of the multishell NTs. A Hitachi S4800 SEM working at 2kV was utilized for the top-view SEM image characterization of the electrodes. Additional morphological and chemical characterization was obtained at the Helios Nanolab 650 FIB-SEM from FEI equipped with an EDX detector from Oxford (Microscopy Service from the University of Malaga). A Tecnai F30 TEM instrument working a 300 kV was utilized for the HAADF-STEM imaging, SAED, and HREM analysis.

The crystalline structure of the electrodes was ascertained by X-ray diffraction in a Panalytical X'PERT PRO model operating in the θ - 2θ configuration and using the Cu Kα (1.5418 Å) radiation as excitation source.

X-ray photoelectron spectroscopy (XPS) analysis of the outer layers of the electrodes to determine the $WO_3/BiVO_4$ coverage ratio and to confirm the chemical state of the oxide semiconductors was carried out in a PHOIBOS 100 hemispheric multichannel analyzer from SPECS, using the Al Kα radiation as excitation source. Low and high resolution spectra were acquired with pass energies of 50 and 30 eV, respectively. Spectra were calibrated positioning the C1s peak at 284.5 eV.

UV-VIS-NIR absorption spectroscopy analysis was carried out recording the diffuse reflectance spectra of the electrodes with a PerkinElmer LAMBDA750S spectrometer equipped with a 60 mm diameter integrating sphere.

Electrochemical and photo-electrochemical analysis and performance

PEC analysis of the multishell NTs and thin film TF reference electrodes was carried out in a three electrodes cell (Redox.me MM PEC 15) supplied with an illumination window (see Supporting

Information, Figure S9 for details). The electrolyte was a 0.5 M Na_2SO_4 solution in Milli-Q DI water. Counter and reference electrodes were a 0.6 mm diameter and 250 mm long Pt wire and an Ag/AgCl (3 M KCl) commercial electrode, respectively. The electrolyte was purged with N_2 during the experiments. All the electrochemical and PEC measurements were performed using a Metrohm Autolab PGSTAT302N potentiostat. The reference electrode voltages and the electrode current density were referred to the RHE and to the geometrical area following the conventions described in reference. [55]

The electrochemical active surface area (ECSA) of the photoelectrodes was estimated following the double-layer capacitance method. [50-53] For that, cyclic voltammetry analysis was performed at different scan rates in the range from 2 to 50 mV/s for a voltage interval comprised between -0.05 and 0.05 mV vs. Ag/AgCl (3 M KCl) reference electrode.

For the PEC characterization studies, photo-anode samples were illuminated from the back side of the substrate. An Oriel Instruments 66921 arc lamp (equipped with an Oriel air mass filter AM1.5 G, reference 81094) and a Mightech PLS-6500 LED lamp were used as sun simulator and 6500K light sources (i.e., blue region of the visible spectrum), respectively. The power flux of these two light sources was adjusted at 100mW/cm^2 by means of a Newport 819C-UV-2-CAL integrating sphere and a 1830R optical power meter. The 6500K LED source provides photons within a defined range of wavelengths between 420 nm and 475 nm, i.e., in the spectral window between the absorption edges of $BiVO_4$ and WO_3 semiconductors (see in Figure S4 the lamp spectral distribution in relation with the diffuse reflectance spectra of the analyzed electrodes). As seen in Figure S4, the choice of the 6500K light-emitting LED for most experiments permitted to selectively excite the $BiVO_4$ semiconductor neglecting any significant contribution to photocurrent due to the direct excitation of the WO_3 semiconductor. In addition, to conform with accepted

practices and established standards of defining electrode performance and wave-length dependence of photocurrent, [55] LSV experiments were also carried out with a standard AM1.5 G solar simulator (ORIEL 66921 arc lamp).

The IPCE response of the multishell NT electrodes was determined at 1.0 V vs RHE using a Zahner CIMPS-QE/IPCE system consisting of a tuneable LED light source (TLS03). The IPCE measurements were performed in a three-electrode cell setup with a platinum foil as the counter electrode and Ag/AgCl (KCl sat.) as a reference electrode. 0.5 M Na_2SO_4 solution was employed as electrolyte. The IPCE values were calculated according to the following equation:

$$= \frac{I(\lambda)}{P \cdot A \cdot \lambda} \cdot \frac{h \cdot c}{q_e} \qquad \text{(Eq. 4)}$$

where ( ) is the photocurrent in A, is the incident light power density in W/m^2 at each wavelength in nm, A is the illuminated area in m^2, h is the Planck constant (6.62607004 × 10^{-34} J s), c is the speed of light (~ 3 × 10^8 m/s), and $_e$ is the electron charge (~1.6 × 10^{-19} C).

Experiments to ascertain the working characteristics of the WO_3/$BiVO_4$ heterojunction as a function of the $BiVO_4$ thickness were carried out by recording LSV (i.e. i-V curves between 0.5 and 1.5 V vs. RHE recorded at a rate of 50 mV/s) and CA (at 1.23 V vs. RHE and for periods of 3 h), under the effect of different illumination conditions with the LED source (dark, light or chopped illumination). Long-term CA experiments were performed at room temperature under the irradiation of a Mightech PLS-6500 LED light source (without UV or NIR wavelength components), while the electrolyte was continuously bubbled with N_2. These illumination and operating conditions prevented heating of the electrolyte. Tafel plots for NT and TF electrodes, the former with and without CoPi co-catalysts, were determined according to the Butler-Volmer equation applied to the recorded LSV diagrams. [54] EIS analysis in the dark and under illumination

was carried out to estimate the characteristics of the charge transfer mechanisms during the OER. Nyquist diagrams were obtained at 1.23 V vs. RHE, applying a 10 mV amplitude sinusoidal signal at frequencies varying from 10^5 Hz to 0.1 Hz. Fitting analysis (Metrohm Autolab NOVA 2.1.4) of these diagrams was done assuming an equivalent circuit similar to that proposed previously for this type of heterojunction electrodes. [26-28]

CONCLUSIONS

The results presented in this work confirm the optimum performance of $BiVO_4$ as an effective sensitizing semiconductor photoanode in combination with WO_3. We have found that NT electrodes, prepared using vacuum deposition procedures and ONWs as substrate-supported soft templates, present a large electrochemically active surface area available for charge transfer reactions. Furthermore, the multishell ITO/WO_3/$BiVO_4$ structure of these electrodes provides very short and equivalent charge pathways to reach the ITO conductive layer all along the complete length of the NTs. It has been also demonstrated that the thickness and homogeneity of the $BiVO_4$ outer shell layer is an additional parameter, which optimized to a value in the range of 65-85 nm, permits to maximize the cell photocurrent.

Within the range of studied photon fluxes, the WO_3/$BiVO_4$ heterojunction structure of the NT electrodes did not present signs of saturation, a feature enabling the use of these electrodes under very high illumination conditions as those provided by solar collector devices. The robust character of the system (it could be reused without any noticeable loss of activity) and its long time stability make these electrodes a suitable option for practical applications. This capacity is further justified by the scalability of the processing methods utilized for their fabrication. Key issues by the utilized synthesis procedure are the use of vacuum processable ONWs as a scaffold and the demonstration

that the MS technique can be used for the preparation of conformal layers of ITO and WO_3 to completely cover 10 microns long NWs. We have also shown that the hollow multishell NT configuration is perfectly compatible with the incorporation of OER co-catalyst. This has been proved by the incorporation of a CoPi layer and the demonstration of an enhancement in PEC efficiency with photocurrents of 2.23 mA/cm^2 at 1.23 V vs. RHE under 1 sun illumination. This value, although not maximal, [22] is within the average of most recent works in the literature. [65] [66] It is expected that thanks to the fine control of the multishell composition, the actual electrochemically active surface area and nanostructure of NTs achieved with the applied synthesis procedure and adapting the co-catslyst application procedure, the PEC efficiency of the cells can be further enhanced.

Supporting Information.

Supporting Information section S1. Experimental Detail for the synthetic protocol.

Supporting Information, complementary Figures S1 to S9. Supporting Information, Table S1.

AUTHOR INFORMATION

Corresponding Author

*Corresponding author: jorge.gil@icmse.csic.es

Jorge Gil-Rostra, Instituto de Ciencia de Materiales de Sevilla (CSIC-US). Avenida de Américo Vespucio, 49, 41092, Sevilla, SPAIN.

Author Contributions

The manuscript was written through the contributions of all authors. All authors have approved the final version of the manuscript.

ACKNOWLEDGMENTS

The authors thank the project PID2019-110430GB-C21 funded by MCIN/AEI/10.13039/501100011033 and by "ERDF (FEDER) A way of making Europe", by the "European Union". The authors also want to thank CSIC for its financial support through the Intramural Project 202260E110. The project leading to this article has received funding from the EU H2020 program under the grant agreement 851929 (ERC Starting Grant 3DScavengers). Authors thank the ICMSE services for Electron Microscopy, X-Ray Diffraction and Surface Analysis, and the Center for Bioinnovation (University of Malaga) for the access to FESEM-FIB.

Table of Contents

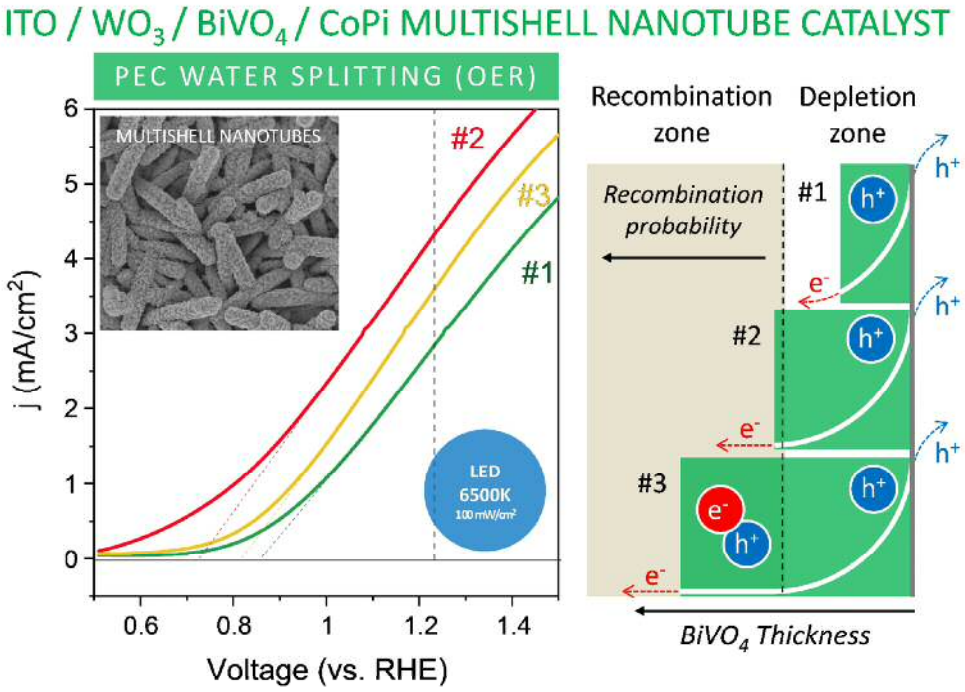

REFERENCES

(1) Soo Han, H.; Shin, S.; Hoe Kim, D.; Jae Park, I.; Seong Kim, J.; Huang, P.-S.; Lee, J.-K.; Sun Cho, I.; Zheng, X. Boosting the Solar Water Oxidation Performance of a BiVO4 Photoanode by Crystallographic Orientation Control. *Energy & Environmental Science* **2018**, *11* (5), 1299–1306. https://doi.org/10.1039/C8EE00125A.

(2) Li, M.; Xiong, Y.; Liu, X.; Bo, X.; Zhang, Y.; Han, C.; Guo, L. Facile Synthesis of Electrospun MFe2O4 (M = Co, Ni, Cu, Mn) Spinel Nanofibers with Excellent Electrocatalytic Properties for Oxygen Evolution and Hydrogen Peroxide Reduction. *Nanoscale* **2015**, *7* (19), 8920–8930. https://doi.org/10.1039/C4NR07243J.

(3) Tang, P.; Xie, H.; Ros, C.; Han, L.; Biset-Peiró, M.; He, Y.; Kramer, W.; Rodríguez, A. P.; Saucedo, E.; Galán-Mascarós, J. R.; Andreu, T.; Morante, J. R.; Arbiol, J. Enhanced Photoelectrochemical Water Splitting of Hematite Multilayer Nanowire Photoanodes by Tuning the Surface State via Bottom-up Interfacial Engineering. *Energy Environ. Sci.* **2017**, *10* (10), 2124–2136. https://doi.org/10.1039/C7EE01475A.

(4) Zhao, B.; Zhang, L.; Zhen, D.; Yoo, S.; Ding, Y.; Chen, D.; Chen, Y.; Zhang, Q.; Doyle, B.; Xiong, X.; Liu, M. A Tailored Double Perovskite Nanofiber Catalyst Enables Ultrafast Oxygen Evolution. *Nat Commun* **2017**, *8* (1), 14586. https://doi.org/10.1038/ncomms14586.

(5) Hong, S. J.; Lee, S.; Jang, J. S.; Lee, J. S. Heterojunction BiVO4/WO3 Electrodes for Enhanced Photoactivity of Water Oxidation. *Energy Environ. Sci.* **2011**, *4* (5), 1781–1787. https://doi.org/10.1039/C0EE00743A.

(6) Wang, W.; Zhang, Y.; Wang, L.; Bi, Y. Facile Synthesis of Fe3+/Fe2+ Self-Doped Nanoporous FeVO4 Photoanodes for Efficient Solar Water Splitting. *J. Mater. Chem. A* **2017**, *5* (6), 2478–2482. https://doi.org/10.1039/C6TA10308A.

(7) Wang, S.; Chen, P.; Yun, J.-H.; Hu, Y.; Wang, L. An Electrochemically Treated BiVO4 Photoanode for Efficient Photoelectrochemical Water Splitting. *Angewandte Chemie International Edition* **2017**, *56* (29), 8500–8504. https://doi.org/10.1002/anie.201703491.

(8) Su, J.; Guo, L.; Bao, N.; Grimes, C. A. Nanostructured WO3/BiVO4 Heterojunction Films for Efficient Photoelectrochemical Water Splitting. *Nano Lett.* **2011**, *11* (5), 1928–1933. https://doi.org/10.1021/nl2000743.

(9) Baek, J. H.; Kim, B. J.; Han, G. S.; Hwang, S. W.; Kim, D. R.; Cho, I. S.; Jung, H. S. BiVO4/WO3/SnO2 Double-Heterojunction Photoanode with Enhanced Charge Separation and Visible-Transparency for Bias-Free Solar Water-Splitting with a Perovskite Solar Cell. *ACS Appl. Mater. Interfaces* **2017**, *9* (2), 1479–1487. https://doi.org/10.1021/acsami.6b12782.

(10) Xu, S.; Fu, D.; Song, K.; Wang, L.; Yang, Z.; Yang, W.; Hou, H. One-Dimensional WO3/BiVO4 Heterojunction Photoanodes for Efficient Photoelectrochemical Water Splitting. *Chemical Engineering Journal* **2018**, *349*, 368–375. https://doi.org/10.1016/j.cej.2018.05.100.

(11) Yang, J. W.; Park, I. J.; Lee, S. A.; Lee, M. G.; Lee, T. H.; Park, H.; Kim, C.; Park, J.; Moon, J.; Kim, J. Y.; Jang, H. W. Near-Complete Charge Separation in Tailored BiVO4-Based Heterostructure Photoanodes toward Artificial Leaf. *Applied Catalysis B: Environmental* **2021**, *293*, 120217. https://doi.org/10.1016/j.apcatb.2021.120217.

(12) Rao, P. M.; Cai, L.; Liu, C.; Cho, I. S.; Lee, C. H.; Weisse, J. M.; Yang, P.; Zheng, X. Simultaneously Efficient Light Absorption and Charge Separation in WO3/BiVO4

Core/Shell Nanowire Photoanode for Photoelectrochemical Water Oxidation. *Nano Lett.* **2014**, *14* (2), 1099–1105. https://doi.org/10.1021/nl500022z.
(13) Zheng, G.; Wang, J.; Liu, H.; Murugadoss, V.; Zu, G.; Che, H.; Lai, C.; Li, H.; Ding, T.; Gao, Q.; Guo, Z. Tungsten Oxide Nanostructures and Nanocomposites for Photoelectrochemical Water Splitting. *Nanoscale* **2019**, *11* (41), 18968–18994. https://doi.org/10.1039/C9NR03474A.
(14) Ibrahim, A. A. M.; Khan, I.; Iqbal, N.; Qurashi, A. Facile Synthesis of Tungsten Oxide – Bismuth Vanadate Nanoflakes as Photoanode Material for Solar Water Splitting. *International Journal of Hydrogen Energy* **2017**, *42* (5), 3423–3430. https://doi.org/10.1016/j.ijhydene.2016.09.095.
(15) Kalanur, S. S.; Hwang, Y. J.; Chae, S. Y.; Joo, O. S. Facile Growth of Aligned WO3 Nanorods on FTO Substrate for Enhanced Photoanodic Water Oxidation Activity. *J. Mater. Chem. A* **2013**, *1* (10), 3479–3488. https://doi.org/10.1039/C3TA01175E.
(16) Ding, J.-R.; Kim, K.-S. 1-D WO3@BiVO4 Heterojunctions with Highly Enhanced Photoelectrochemical Performance. *Chemical Engineering Journal* **2018**, *334*, 1650–1656. https://doi.org/10.1016/j.cej.2017.11.130.
(17) Lee, B. R.; Lee, M. G.; Park, H.; Lee, T. H.; Lee, S. A.; Bhat, S. S. M.; Kim, C.; Lee, S.; Jang, H. W. All-Solution-Processed WO3/BiVO4 Core–Shell Nanorod Arrays for Highly Stable Photoanodes. *ACS Appl. Mater. Interfaces* **2019**, *11* (22), 20004–20012. https://doi.org/10.1021/acsami.9b03712.
(18) Wei, P.; Wen, Y.; Lin, K.; Li, X. 2D/3D WO3/BiVO4 Heterostructures for Efficient Photoelectrocatalytic Water Splitting. *International Journal of Hydrogen Energy* **2021**, *46* (54), 27506–27515. https://doi.org/10.1016/j.ijhydene.2021.06.007.
(19) Ma, H.; Zhang, J.; Liu, Z. Efficient Tungsten Oxide/Bismuth Oxyiodide Core/Shell Photoanode for Photoelectrochemical Water Splitting. *Applied Surface Science* **2017**, *423*, 63–70. https://doi.org/10.1016/j.apsusc.2017.06.121.
(20) Bielinski, A. R.; Lee, S.; Brancho, J. J.; Esarey, S. L.; Gayle, A. J.; Kazyak, E.; Sun, K.; Bartlett, B. M.; Dasgupta, N. P. Atomic Layer Deposition of Bismuth Vanadate Core–Shell Nanowire Photoanodes. *Chem. Mater.* **2019**, *31* (9), 3221–3227. https://doi.org/10.1021/acs.chemmater.9b00065.
(21) Shi, X.; Choi, I. Y.; Zhang, K.; Kwon, J.; Kim, D. Y.; Lee, J. K.; Oh, S. H.; Kim, J. K.; Park, J. H. Efficient Photoelectrochemical Hydrogen Production from Bismuth Vanadate-Decorated Tungsten Trioxide Helix Nanostructures. *Nat Commun* **2014**, *5* (1), 4775. https://doi.org/10.1038/ncomms5775.
(22) Kalanoor, B. S.; Seo, H.; Kalanur, S. S. Recent Developments in Photoelectrochemical Water-Splitting Using WO3/BiVO4 Heterojunction Photoanode: A Review. *Materials Science for Energy Technologies* **2018**, *1* (1), 49–62. https://doi.org/10.1016/j.mset.2018.03.004.
(23) López-Fernández, E.; Gil-Rostra, J.; Espinós, J. P.; González-Elipe, A. R.; de Lucas Consuegra, A.; Yubero, F. Chemistry and Electrocatalytic Activity of Nanostructured Nickel Electrodes for Water Electrolysis. *ACS Catal.* **2020**, *10* (11), 6159–6170. https://doi.org/10.1021/acscatal.0c00856.
(24) Selim, S.; Francàs, L.; García-Tecedor, M.; Corby, S.; Blackman, C.; Gimenez, S.; Durrant, J. R.; Kafizas, A. WO3/BiVO4: Impact of Charge Separation at the Timescale of Water Oxidation. *Chem. Sci.* **2019**, *10* (9), 2643–2652. https://doi.org/10.1039/C8SC04679D.

(25) Grigioni, I.; Polo, A.; Dozzi, M. V.; Stamplecoskie, K. G.; Jara, D. H.; Kamat, P. V.; Selli, E. Enhanced Charge Carrier Separation in WO3/BiVO4 Photoanodes Achieved via Light Absorption in the BiVO4 Layer. *ACS Appl. Energy Mater.* **2022**, *5* (11), 13142–13148. https://doi.org/10.1021/acsaem.2c02597.
(26) Bredar, A. R. C.; Chown, A. L.; Burton, A. R.; Farnum, B. H. Electrochemical Impedance Spectroscopy of Metal Oxide Electrodes for Energy Applications. *ACS Appl. Energy Mater.* **2020**, *3* (1), 66–98. https://doi.org/10.1021/acsaem.9b01965.
(27) Shi, Q.; Murcia-López, S.; Tang, P.; Flox, C.; Morante, J. R.; Bian, Z.; Wang, H.; Andreu, T. Role of Tungsten Doping on the Surface States in BiVO4 Photoanodes for Water Oxidation: Tuning the Electron Trapping Process. *ACS Catal.* **2018**, *8* (4), 3331–3342. https://doi.org/10.1021/acscatal.7b04277.
(28) Bertoluzzi, L.; Lopez-Varo, P.; Tejada, J. A. J.; Bisquert, J. Charge Transfer Processes at the Semiconductor/Electrolyte Interface for Solar Fuel Production: Insight from Impedance Spectroscopy. *J. Mater. Chem. A* **2016**, *4* (8), 2873–2879. https://doi.org/10.1039/C5TA03210E.
(29) Watzele, S.; Hauenstein, P.; Liang, Y.; Xue, S.; Fichtner, J.; Garlyyev, B.; Scieszka, D.; Claudel, F.; Maillard, F.; Bandarenka, A. S. Determination of Electroactive Surface Area of Ni-, Co-, Fe-, and Ir-Based Oxide Electrocatalysts. *ACS Catal.* **2019**, *9* (10), 9222–9230. https://doi.org/10.1021/acscatal.9b02006.
(30) Liu, J.; Yang, Q.; Liu, J.; Luo, H. Enhanced Photoelectrochemical Water Oxidation of WO3/R-CoO and WO3/B-CoO Photoanodes with a Type II Heterojunction. *J Mater Sci* **2021**, *56* (13), 8079–8090. https://doi.org/10.1007/s10853-020-05754-5.
(31) Liu, J.; Chen, W.; Sun, Q.; Zhang, Y.; Li, X.; Wang, J.; Wang, C.; Yu, Y.; Wang, L.; Yu, X. Oxygen Vacancies Enhanced WO3/BiVO4 Photoanodes Modified by Cobalt Phosphate for Efficient Photoelectrochemical Water Splitting. *ACS Appl. Energy Mater.* **2021**, *4* (3), 2864–2872. https://doi.org/10.1021/acsaem.1c00145.
(32) Yoon, S.-H.; Sadike, T.; Ding, J.-R.; Kim, K.-S. Photoelectrochemical Oxygen Evolution with Cobalt Phosphate and BiVO4 Modified 1-D WO3 Prepared by Flame Vapor Deposition. *Journal of Industrial and Engineering Chemistry* **2020**, *85*, 240–248. https://doi.org/10.1016/j.jiec.2020.02.006.
(33) Pilli, S. K.; Janarthanan, R.; Deutsch, T. G.; Furtak, T. E.; Brown, L. D.; Turner, J. A.; Herring, A. M. Efficient Photoelectrochemical Water Oxidation over Cobalt-Phosphate (Co-Pi) Catalyst Modified BiVO4/1D-WO3 Heterojunction Electrodes. *Phys. Chem. Chem. Phys.* **2013**, *15* (35), 14723–14728. https://doi.org/10.1039/C3CP52401A.
(34) Pilli, S. K.; Furtak, T. E.; Brown, L. D.; Deutsch, T. G.; Turner, J. A.; Herring, A. M. Cobalt-Phosphate (Co-Pi) Catalyst Modified Mo-Doped BiVO4 Photoelectrodes for Solar Water Oxidation. *Energy Environ. Sci.* **2011**, *4* (12), 5028–5034. https://doi.org/10.1039/C1EE02444B.
(35) Castillo-Seoane, J.; Gil-Rostra, J.; López-Flores, V.; Lozano, G.; Ferrer, F. J.; Espinós, J. P.; Ostrikov, K. (Ken); Yubero, F.; González-Elipe, A. R.; Barranco, Á.; Sánchez-Valencia, J. R.; Borrás, A. One-Reactor Vacuum and Plasma Synthesis of Transparent Conducting Oxide Nanotubes and Nanotrees: From Single Wire Conductivity to Ultra-Broadband Perfect Absorbers in the NIR. *Nanoscale* **2021**, *13* (32), 13882–13895. https://doi.org/10.1039/D1NR01937F.
(36) Filippin, A. N.; Macias-Montero, M.; Saghi, Z.; Idígoras, J.; Burdet, P.; Barranco, A.; Midgley, P.; Anta, J. A.; Borras, A. Vacuum Template Synthesis of Multifunctional

Nanotubes with Tailored Nanostructured Walls. *Sci Rep* **2016**, *6* (1), 20637. https://doi.org/10.1038/srep20637.
(37) Filippin, A. N.; Sanchez-Valencia, J. R.; Idígoras, J.; Rojas, T. C.; Barranco, A.; Anta, J. A.; Borras, A. Plasma Assisted Deposition of Single and Multistacked TiO2 Hierarchical Nanotube Photoanodes. *Nanoscale* **2017**, *9* (24), 8133–8141. https://doi.org/10.1039/C7NR00923B.
(38) Borras, A.; Gröning, O.; Aguirre, M.; Gramm, F.; Gröning, P. One-Step Dry Method for the Synthesis of Supported Single-Crystalline Organic Nanowires Formed by π-Conjugated Molecules. *Langmuir* **2010**, *26* (8), 5763–5771. https://doi.org/10.1021/la1003758.
(39) Filippin, A. N.; López-Flores, V.; Rojas, T. C.; Saghi, Z.; Rico, V. J.; Sanchez-Valencia, J. R.; Espinós, J. P.; Zitolo, A.; Viret, M.; Midgley, P. A.; Barranco, A.; Borras, A. Self-Assembly of the Nonplanar Fe(III) Phthalocyanine Small-Molecule: Unraveling the Impact on the Magnetic Properties of Organic Nanowires. *Chem. Mater.* **2018**, *30* (3), 879–887. https://doi.org/10.1021/acs.chemmater.7b04515.
(40) Louloudakis, D.; Mouratis, K.; Gil-Rostra, J.; Koudoumas, E.; Alvarez, R.; Palmero, A.; Gonzalez-Elipe, A. R. Electrochromic Response and Porous Structure of WO3 Cathode Layers. *Electrochimica Acta* **2021**, *376*, 138049. https://doi.org/10.1016/j.electacta.2021.138049.
(41) Pihosh, Y.; Turkevych, I.; Mawatari, K.; Asai, T.; Hisatomi, T.; Uemura, J.; Tosa, M.; Shimamura, K.; Kubota, J.; Domen, K.; Kitamori, T. Nanostructured WO3/BiVO4 Photoanodes for Efficient Photoelectrochemical Water Splitting. *Small* **2014**, *10* (18), 3692–3699. https://doi.org/10.1002/smll.201400276.
(42) Pihosh, Y.; Turkevych, I.; Mawatari, K.; Uemura, J.; Kazoe, Y.; Kosar, S.; Makita, K.; Sugaya, T.; Matsui, T.; Fujita, D.; Tosa, M.; Kondo, M.; Kitamori, T. Photocatalytic Generation of Hydrogen by Core-Shell WO3/BiVO4 Nanorods with Ultimate Water Splitting Efficiency. *Sci Rep* **2015**, *5* (1), 11141. https://doi.org/10.1038/srep11141.
(43) Kalanur, S. S.; Yoo, I.-H.; Park, J.; Seo, H. Insights into the Electronic Bands of WO3/BiVO4/TiO2, Revealing High Solar Water Splitting Efficiency. *J. Mater. Chem. A* **2017**, *5* (4), 1455–1461. https://doi.org/10.1039/C6TA07592D.
(44) Macias-Montero, M.; Filippin, A. N.; Saghi, Z.; Aparicio, F. J.; Barranco, A.; Espinos, J. P.; Frutos, F.; Gonzalez-Elipe, A. R.; Borras, A. Vertically Aligned Hybrid Core/Shell Semiconductor Nanowires for Photonics Applications. *Advanced Functional Materials* **2013**, *23* (48), 5981–5989. https://doi.org/10.1002/adfm.201301120.
(45) Moore, K.; Clemons, C. B.; Kreider, K. L.; Young, G. W. Modeling and Simulation of Axisymmetric Coating Growth on Nanofibers. *Journal of Applied Physics* **2007**, *101* (6), 064305. https://doi.org/10.1063/1.2710442.
(46) Alvarez, R.; González-Elipe, A. R.; Palmero, *A. Deposition of Porous Nanocolumnar Thin Films by Magnetron Sputtering*. In *Plasma Applications for Material Modification*; Jenny Stanford Publishing, **2021**, 55–97. https://doi.org/10.1201/9781003119203.
(47) Lee, J.-H. Effects of Substrate Temperature on Electrical and Optical Properties ITO Films Deposited by r.f. Magnetron Sputtering. *J Electroceram* **2008**, *23* (2), 554. https://doi.org/10.1007/s10832-008-9539-6.
(48) Gullapalli, S. K.; Vemuri, R. S.; Ramana, C. V. Structural Transformation Induced Changes in the Optical Properties of Nanocrystalline Tungsten Oxide Thin Films. *Appl. Phys. Lett.* **2010**, *96* (17), 171903. https://doi.org/10.1063/1.3421540.

(49) Luo, H.; Mueller, A. H.; McCleskey, T. M.; Burrell, A. K.; Bauer, E.; Jia, Q. X. Structural and Photoelectrochemical Properties of BiVO4 Thin Films. *J. Phys. Chem. C* **2008**, *112* (15), 6099–6102. https://doi.org/10.1021/jp7113187.
(50) Xiong, S.; Li, P.; Jin, Z.; Gao, T.; Wang, Y.; Guo, Y.; Xiao, D. Enhanced Catalytic Performance of ZnO-CoOx Electrode Generated from Electrochemical Corrosion of Co-Zn Alloy for Oxygen Evolution Reaction. *Electrochimica Acta* **2016**, *222*, 999–1006. https://doi.org/10.1016/j.electacta.2016.11.068.
(51) Vincent, I. Electrochemical Characterization and Oxygen Reduction Kinetics of Cu-Incorporated Cobalt Oxide Catalyst. *Int. J. Electrochem. Sci.* **2016**, 8002–8015. https://doi.org/10.20964/2016.09.12.
(52) Sun, M.; Wang, Z.; Gao, B.; Wang, S.; Wang, C.; Song, X.; Lin, D. Electrocatalytic Hydrogen Evolution Properties of Anionic NiS2-Ni(OH)2 Nanosheets Produced on the Surface of Nickel Foam. *International Journal of Energy Research* **2020**, *44* (6), 4827–4836. https://doi.org/10.1002/er.5275.
(53) Mohite, S. V.; Xing, R.; Li, B.; Latthe, S. S.; Zhao, Y.; Li, X.; Mao, L.; Liu, S. Spatial Compartmentalization of Cobalt Phosphide in P-Doped Dual Carbon Shells for Efficient Alkaline Overall Water Splitting. *Inorg. Chem.* **2020**, *59* (3), 1996–2004. https://doi.org/10.1021/acs.inorgchem.9b03363.
(54) Shombe, G. B.; Khan, M. D.; Zequine, C.; Zhao, C.; Gupta, R. K.; Revaprasadu, N. Direct Solvent Free Synthesis of Bare α-NiS, β-NiS and α-β-NiS Composite as Excellent Electrocatalysts: Effect of Self-Capping on Supercapacitance and Overall Water Splitting Activity. *Sci Rep* **2020**, *10* (1), 3260. https://doi.org/10.1038/s41598-020-59714-9.
(55) Chen, Z.; Jaramillo, T. F.; Deutsch, T. G.; Kleiman-Shwarsctein, A.; Forman, A. J.; Gaillard, N.; Garland, R.; Takanabe, K.; Heske, C.; Sunkara, M.; McFarland, E. W.; Domen, K.; Miller, E. L.; Turner, J. A.; Dinh, H. N. Accelerating Materials Development for Photoelectrochemical Hydrogen Production: Standards for Methods, Definitions, and Reporting Protocols. *Journal of Materials Research* **2010**, *25* (1), 3–16. https://doi.org/10.1557/JMR.2010.0020.
(56) Valdés, Á.; Qu, Z.-W.; Kroes, G.-J.; Rossmeisl, J.; Nørskov, J. K. Oxidation and Photo-Oxidation of Water on TiO2 Surface. *J. Phys. Chem. C* **2008**, *112* (26), 9872–9879. https://doi.org/10.1021/jp711929d.
(57) Rossmeisl, J.; Qu, Z.-W.; Zhu, H.; Kroes, G.-J.; Nørskov, J. K. Electrolysis of Water on Oxide Surfaces. *Journal of Electroanalytical Chemistry* **2007**, *607* (1), 83–89. https://doi.org/10.1016/j.jelechem.2006.11.008.
(58) Kanan, M. W.; Yano, J.; Surendranath, Y.; Dincă, M.; Yachandra, V. K.; Nocera, D. G. Structure and Valency of a Cobalt−Phosphate Water Oxidation Catalyst Determined by in Situ X-Ray Spectroscopy. *J. Am. Chem. Soc.* **2010**, *132* (39), 13692–13701. https://doi.org/10.1021/ja1023767.
(59) Surendranath, Y.; Lutterman, D. A.; Liu, Y.; Nocera, D. G. Nucleation, Growth, and Repair of a Cobalt-Based Oxygen Evolving Catalyst. *J. Am. Chem. Soc.* **2012**, *134* (14), 6326–6336. https://doi.org/10.1021/ja3000084.
(60) Ibadurrohman, M.; Hellgardt, K. Photoelectrochemical Performance of Graphene-Modified TiO2 Photoanodes in the Presence of Glycerol as a Hole Scavenger. *International Journal of Hydrogen Energy* **2014**, *39* (32), 18204–18215. https://doi.org/10.1016/j.ijhydene.2014.08.142.

(61) Liu, Y.; Li, J.; Li, W.; Yang, Y.; Li, Y.; Chen, Q. Enhancement of the Photoelectrochemical Performance of WO3 Vertical Arrays Film for Solar Water Splitting by Gadolinium Doping. *J. Phys. Chem. C* **2015**, *119* (27), 14834–14842. https://doi.org/10.1021/acs.jpcc.5b00966.
(62) Martin, M. H.; Lasia, A. Influence of Experimental Factors on the Constant Phase Element Behavior of Pt Electrodes. *Electrochimica Acta* **2011**, *56* (23), 8058–8068. https://doi.org/10.1016/j.electacta.2011.02.068.
(63) Holm, S.; Holm, T.; Martinsen, Ø. G. Simple Circuit Equivalents for the Constant Phase Element. *PLOS ONE* **2021**, *16* (3), e0248786. https://doi.org/10.1371/journal.pone.0248786.
(64) Romero-Gomez, P.; Borras, A.; Barranco, A.; Espinos, J. P.; Gonzalez-Elipe, A. R. Enhanced Photoactivity in Bilayer Films with Buried Rutile–Anatase Heterojunctions. *ChemPhysChem* **2011**, *12* (1), 191–196. https://doi.org/10.1002/cphc.201000734.
(65) Xu, S.; Fu, D.; Song, K.; Wang, L.; Yang, Z.; Yang, W.; Hou, H. One-Dimensional WO3/BiVO4 Heterojunction Photoanodes for Efficient Photoelectrochemical Water Splitting. *Chemical Engineering Journal* **2018**, *349*, 368–375. https://doi.org/10.1016/j.cej.2018.05.100.
(66) Ma, Z.; Song, K.; Wang, L.; Gao, F.; Tang, B.; Hou, H.; Yang, W. WO3/BiVO4 Type-II Heterojunction Arrays Decorated with Oxygen-Deficient ZnO Passivation Layer: A Highly Efficient and Stable Photoanode. *ACS Appl. Mater. Interfaces* **2019**, *11* (1), 889–897. https://doi.org/10.1021/acsami.8b18261.